



OPEN

Nanoscale mechanical contacts mapped by ultrashort time-scale electron transport

SUBJECT AREAS:
NANOSCALE MATERIALS
MATERIALS SCIENCE

Motonobu Tomoda¹, Thomas Dehoux², Yohei Iwasaki¹, Osamu Matsuda¹, Vitalyi E. Gusev³
& Oliver B. Wright¹

Received
27 December 2013

Accepted
21 March 2014

Published
25 April 2014

Correspondence and
requests for materials
should be addressed to
M.T. (mtomoda@eng.
hokudai.ac.jp)

¹Division of Applied Physics, Faculty of Engineering, Hokkaido University, Sapporo, 060-8628, Japan, ²Univ. Bordeaux, CNRS, I2M, UMR 5295, F-33405 Talence, France, ³LAUM, UMR CNRS 6613, Université du Maine, LUNAM Université, Av. O. Messiaen, 72085 Le Mans, France.

Mechanical contacts are crucial to systems in engineering, electronics and biology. The microscopic nature of the contacting surfaces determines how they mesh on the nanoscale. There is thus much interest in methods that can map the actual area of two surfaces in contact—the real contact area—during the loading or unloading phases. We address this problem using an ultrafast optical technique to generate non-equilibrium electrons that diffuse across a nanoscale mechanical contact between two thin gold films deposited on sapphire. We image this process in the contact and near-contact regions to micron resolution *in situ* using transient optical reflectivity changes on femtosecond time scales. By use of a model of the ultrashort-time electron dynamics, we account for an up to ~40% drop in the transient optical reflectivity change on contact. We thereby show how the real contact area of a nanoscale contact can be mapped. Applications include the probing of microelectronic mechanical devices.

Mechanical contacts between solids rely on the meshing of individual asperities on the nanoscale. Such contacts govern the phenomena of friction and lubrication, and are exquisitely sensitive to the surface roughness and to the state of the surface¹. Elastic and plastic behaviors are often studied with micro- or macroscale indenters^{1,2}, but this does not allow the physics of the deformation process to be studied locally and during loading. One can image nanoindentation processes with nanoscale resolution in a transmission electron microscope, but this is not suited to continuous mapping over the contact area during deformation³. Neither does it provide a measure of the microscopic (i.e. real) area of contact, a quantity of vital importance in understanding adhesion and friction.

The contact area can be directly imaged by ultrasonic, thermal or optical methods^{4–10}. Ultrasonic methods have two advantages: they may be used to map opaque materials over the whole contact area, and, if very high ultrasonic frequencies are implemented, they potentially allow nanoscale spatial resolution in the through-contact direction^{6,7}. However, it is hard to relate ultrasonic reflection or transmission coefficients quantitatively to the real microscopic contact area. Likewise, mapping with thermal waves involves heat conduction through asperities as well as through the gaps between them, again rendering it difficult to measure this area^{6,7}. Probing the real contact area in transparent solids in static or frictional contact using optical methods is also feasible^{8–10}, but these methods are limited by the finite optical wavelength to samples with roughness ≥ 50 nm.

Here we propose a way to map the real contact area of nanoscale contacts: we investigate the mechanical contact between metal-coated materials *in situ* by the use of optically-excited electron transport probed on sub-picosecond time scales. Ultrafast non-equilibrium electron diffusion in metals has been extensively studied by ultrashort-time-scale transient optical reflectivity measurements^{11–22}, and such techniques have been implemented to image buried metallic layers²³. We harness such electrons here to map the mechanical contact between a gold-coated sphere and a gold-coated plane (a Hertzian-contact geometry), offering the crucial advantage of mapping of a nanoscale mechanical contact during loading: for separations greater than angstrom-order, the electrons cannot cross the gaps between the contacting solids, and so allow the selective sensing of the real contact area. This sensing we achieve by implementing an analytical model for the diffusion of non-equilibrium electrons through the contacting nano-asperities.



Results

Samples and single-point transient reflectivity measurements.

Gold films of thickness 37 nm are sputtered onto a sapphire sphere of diameter 2 mm and a sapphire plate of thickness 1 mm. The rms (root mean square) surface roughnesses measured by atomic force microscopy (AFM) are $\sigma_s = 1.9$ and $\sigma_i = 1.6$ nm (error $\pm 20\%$) for the coated plate and sphere, respectively, as shown by typical traces in Fig. 1(b) and (c) and by the corresponding power spectral densities (PSD) in Fig. 1(d) and (e). The sapphire plate is fixed horizontally on a rigid holder, pierced to allow optical access through the plate to the sapphire/gold interface, as shown in Fig. 1(a). The sphere is pressed against the plate, both with vertical (0001) principal crystal axes, using a displacement stage, and the load is monitored with a load cell.

We use an optical pump-probe technique with ~ 200 fs duration pulses of repetition frequency 80 MHz and wavelength 830 nm from a mode-locked Ti:Sapphire laser. The focused pump-beam photons excite electrons in the gold film on the sapphire plate to non-equilibrium states within a distance from the sapphire/gold interface of the order of the optical absorption depth ($\zeta_{\text{pump}} \approx 12 \text{ nm}^{24}$). These electrons subsequently diffuse into the gold film, probing the mechanical contact when they reach the contacting interface, and decay to thermal phonons to produce a transient lattice temperature rise. The optical reflectivity change of the probe beam at wavelength 415 nm

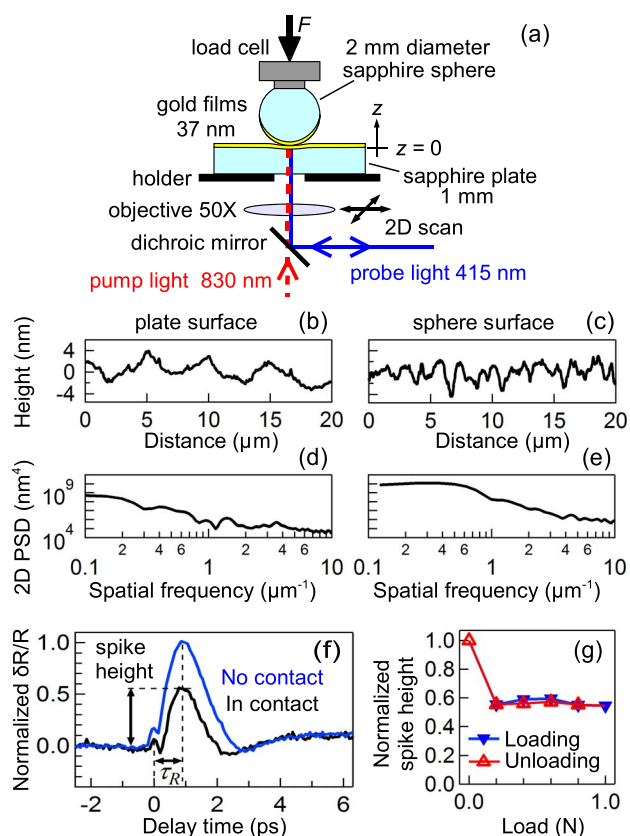


Figure 1 | Experimental setup, typical AFM data, and single-point transient reflectivity results. (a) Experimental setup. The arrow indicates the applied load. (b) AFM trace for the gold-coated sapphire plate (before indentation). (c) AFM trace for the gold-coated sapphire sphere (before indentation). (d), (e) Two-dimensional isotropic power spectral densities (2D PSD) of the AFM images for the gold-coated sapphire plate and sphere, respectively (before indentation). (f) Normalized relative reflectivity variation at load $F = 0.6$ N (in contact for loading: black line) and $F = 0$ N (no contact: blue line) vs. delay time. A constant background contribution from thermoreflectance has been subtracted. (g) Normalized spike height plotted against load for loading and subsequent unloading.

(where $\zeta_{\text{probe}} \approx 17 \text{ nm}^{24}$) is coupled through induced changes in the complex refractive index to the non-equilibrium electron distribution. Image data with $\sim 1 \mu\text{m}$ spatial resolution is obtained by scanning the coaxial optical spots laterally in two dimensions over the circular contact area.

We first selected the point on the sample corresponding to the center of the mechanical contact, and scanned the delay time t on changing the load F . Figure 1(f) shows the probe relative-reflectivity change $\delta R/R$ at $F = 0$ (i.e. before contact with the sample) and at $F = 0.6$ N on loading. A small peak in the reflectivity change is visible centred at $t = 0$, that we believe to be caused by transitions from sharp maxima in the electron density of states²⁵ to states ~ 1 eV above and below the Fermi level. The lifetime of the photoexcited electrons in these states is shorter than 10 fs, and they should cause a reflectance change only when the pump and probe pulses temporally overlap. (This represents a precise measure of the $t = 0$ time delay.) We also observe a spike at $t \approx 0.9$ ps, a time we term τ_R , owing to the excitation of non-equilibrium electrons. One can see that the effect of loading is to dramatically reduce this spike height to ~ 0.6 of that out of contact. (τ_R was independent of loading.) At longer times (3–6 ps) there is a smaller rise in $\delta R/R$ owing to the transient lattice temperature change $\Delta T_l \sim 3$ K and residual photoelastic effects. (Small acoustic oscillations after this time allow a determination of the film thickness.) We may ignore these residual photoelastic effects at short times because of the relatively low value of the heat capacity of the electrons¹⁵.

We define the spike height at τ_R as the difference between the relative reflectivity change at the spike and before the pump-pulse arrival, $\delta R/R|_{t=\tau_R} - \delta R/R|_{t=-1 \text{ ps}} \sim 10^{-5}$. For our 3.0 eV probe pulses exciting d -state electrons in gold at ~ 3.075 eV below the Fermi level, the spike height can be considered to be a measure of the non-equilibrium electron quantum-state occupancy (i.e. electron density) of optically-probed state energies $E \sim 0.075$ eV below the Fermi level—see the Supplementary Information. At this probe energy the value of τ_R is approximately twice that for the case of infrared probing. (Photon energy 3 eV is larger than the highest value, 2.68 eV, reported for sub-picosecond-resolution experiments on gold¹³. Transient reflectivity signals at 2.84 eV and 3.06 eV have been reported with ~ 1.5 ps time resolution²⁰.)

Figure 1(g) shows spike-height data at the center of the contact area when loading up to 1.0 N and then unloading, in steps of 0.2 N for a pristine region of the sample. These curves represent the ratio of the spike heights in and out of contact, and we term this quantity the normalized spike height. One can see that loading even by 0.2 N produces a substantial drop in spike height. The relatively low level of hysteresis, below the experimental error, suggests that one can apply models based on elastic deformation to describe the contact mechanics to a first approximation.

Transient reflectivity imaging over the contact. The ultrafast electronic response can be mapped over the contact area by laterally scanning the pump and probe spot positions. The static probe reflectivity R also depends on position, and we shall consider R first: Figure 2(a) shows an image for R for a $56 \times 56 \mu\text{m}^2$ region at 1.0 N load (measured simultaneously with δR) together with a horizontal cross section through the center of the image. The concentric circles are Newton's rings caused by probe beam interference in the gap between the gold films outside the contact region^{6,7}. The central region inside the rings includes the contact area.

Hertz theory¹ for the elastic deformation of a sphere of radius R_0 indenting a frictionless half-space gives, for the contact radius a , $a^3 = 3FR_0/4E^*$, where $E^* = [(1-\nu_i^2)/E_i + (1-\nu_s^2)/E_s]^{-1}$ is the effective modulus of the indenter (i) and substrate (s), and $\nu_{i,s}$ and $E_{i,s}$ are Poisson's ratios and Young's moduli, respectively. Outside the contact area, the air gap $\Delta d(r)$ between the sphere and the substrate (i.e. plate) is given as a function of radial distance r for $r > a$ by¹

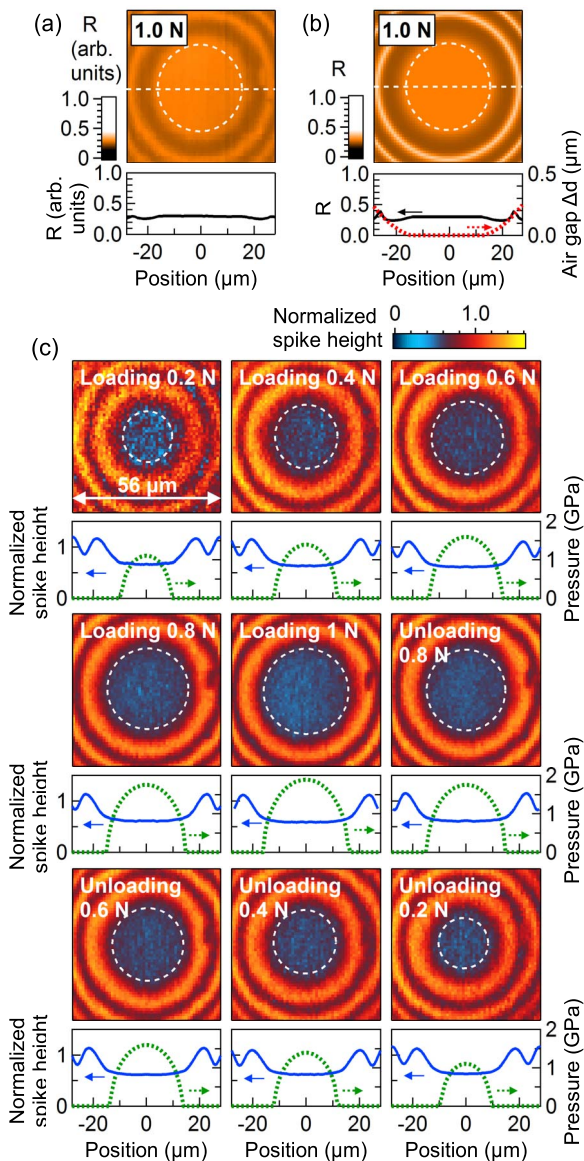


Figure 2 | Mapping the reflectivity and ultrafast reflectivity changes over the contact area, and comparison of the contact area with Hertz theory. (a) Measured probe light reflectivity R images for a $56 \times 56 \mu\text{m}^2$ region around the contact area and cross sections for 1 N loading. Absolute calibration is obtained from (b). (b) Calculated R image and its cross section (solid line) for 1 N loading, and calculated air gap between the sphere and plate (dotted line). (c) Normalized spike-height images and, shown below each image, their cross sections (solid lines, azimuthally-averaged) and calculated contact pressure profiles (dotted lines). The dashed rings in (a)–(c) show the fitted contact areas.

$$\Delta d(r) = R_0 - \sqrt{R_0^2 - r^2} - \frac{1}{\pi R_0} \left[(2a^2 - r^2) \sin^{-1} \left(\frac{a}{r} \right) + a \sqrt{r^2 - a^2} \right]. \quad (1)$$

We calculated the Newton's ring patterns using Eq. (1) by the use of parallel-surface multiple-beam reflection theory for the probe beam, taking into account the known refractive indices of gold and sapphire²⁴, but using E^* as a fitting parameter. Figure 2(b) shows a calculated image for R at 1.0 N load and its horizontal cross section (solid line) using $E^* = 187 \pm 5$ GPa obtained from an average of a series of measurements at different loads up to 1.0 N. Reasonable agreement in both contrast and spacing is obtained. This value of E^*

is 0.8 times that (233 GPa) of a sapphire-sapphire contact²⁶, and 2.2 times that (85 GPa) of a more compliant gold-gold contact²⁷. This is as expected given the softening of the contact owing to the gold films^{28,29}. Figure 2(b) also shows the calculated Δd (dotted line) obtained from Eq. (1). The calculated contact areas are shown by the dashed rings in these images.

We now present imaging of the ultrafast electronic response derived from data at $t = \tau_R$ and -1 ps. Figure 2(c) shows normalized spike-height images for the same region as Fig. 2(a) when loading up to 1 N and then unloading, for a pristine region of the sample. As expected from the results of Fig. 1(g), hysteresis in the images for loading and unloading is negligible. The azimuthally-averaged cross sections are shown in the plots below each image (solid lines). Newton's rings for the probe light remain in the normalized quantity $\delta R/R$, because the effect of the probe optical interference in the gap region outside the contact differs for R and δR ³⁰. (Pump light can also cause Newton's rings, but the effect is small here because of the smaller optical absorption depth.)

The Hertz pressure distribution $p(r) = p_0[1 - (r/a)^2]^{1/2}$ takes a maximum value $p_0 = 3F/2\pi a^2$ at $r = 0$. The calculated contact areas and pressure distributions are shown respectively by the dashed rings in the images of Fig. 2(c) and the dotted lines in the cross sections. We estimate $a = 9.3 \mu\text{m}$ and $p_0 = 1.1$ GPa at the lowest loads (0.2 N), whereas $a = 15.9 \mu\text{m}$ and $p_0 = 1.9$ GPa at the highest loads (1 N) (with corresponding plate indentations $\delta_0 = a^2/R_0 \sim 85$ and 250 nm, respectively). In contrast, the gold film maximum indentations are expected to be much smaller (and in any case small compared to the film thickness), and will be neglected in the analysis in this paper. (We estimate the combined change in film thickness at the center of the contact area at 1 N load owing to elastic and plastic deformations to be ~ 2 nm.) To apply Hertz theory, the combined surface roughness $\sigma = (\sigma_i^2 + \sigma_s^2)^{1/2} \approx 2.5$ nm of the contacting surfaces should also be considered. In our case the parameter $\alpha = \sigma/\delta_0 < 0.03 \ll 1$ for $F > 0.2$ N, so modifications of Hertz theory to account for surface roughness are unnecessary¹.

The spatially-resolved data of Fig. 2(c) represents a wide range of pressures, even for a fixed load F . For each F we sample the data in $1 \mu\text{m}$ steps in the radial direction for $r < 0.95a$. The results for the normalized spike height are plotted in Fig. 3(c) as a function of

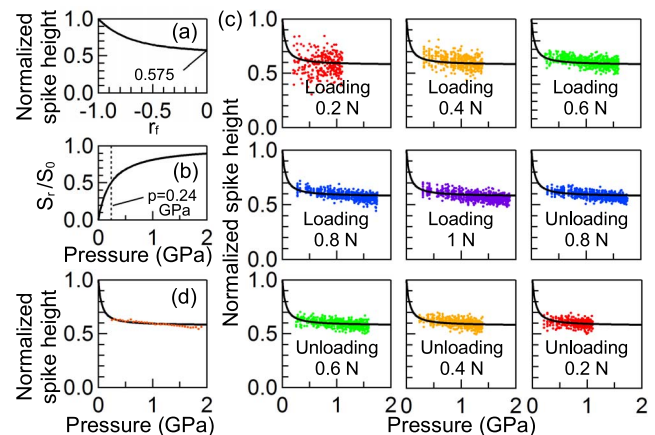


Figure 3 | Relating the ultrafast reflectivity changes to the pressure and real contact area. (a) Theoretical normalized spike height, $\Psi_{r_j}(0, \tau_R)/\Psi(0, \tau_R)$, plotted as a function of r_f . (b) Plot of the assumed variation of the ratio of the real to nominal contact area S_r/S_0 as a function of the pressure p , assuming the relation $S_r/S_0 = p/(p + H)$. The vertical dotted line represents the hardness H fitted from all our data. (c) Measured normalized spike-height vs calculated pressure p , obtained from the data of Fig. 2(c). The solid curves are fitted from theory, assuming $H = 0.24$ GPa. (d) Combined data (dotted curve) from the 9 plots in (c) together with theoretical fit (solid curve).



pressure. Apart from the lower pressures, the value of the normalized spike height is again very close to 0.6.

Analytical model of the electron diffusion. To understand these results one must first consider the dynamics of transiently heated electrons in gold. A one-dimensional (1D) model of the electron diffusion is appropriate because the electron diffusion length (~ 100 nm—see below) is much smaller than the optical spot sizes (~ 1 μm)^{21,22}. The non-equilibrium electron diffusivity is $D_e = \kappa/C_e \approx 1.56 \times 10^{-2}$ m²/s, where $\kappa = 317$ W/m K is the equilibrium thermal conductivity and C_e the electron specific heat²²: $C_e = \gamma T_b$, where the constant coefficient $\gamma \approx 68$ J/m³K² and the lattice temperature $T_l \approx 300$ K. The electron diffusion length, $\sim \sqrt{D_e \tau_R} \sim 140$ nm, significantly exceeds the probe absorption depth $\zeta \approx 17$ nm²⁴. For films of thickness $d \geq 2\zeta$, as in our case, it is therefore reasonable when calculating electron diffusion to make the approximation of surface absorption of the photon energy.

We proceed by assuming that the spatiotemporal variation of the non-equilibrium electron density contains a term $\Psi(z, t)$ that obeys the 1D diffusion equation²². The electron density is obtained by multiplying this term by the temporal form of the solution for homogeneous excitation in the absence of diffusion. For an infinite half-space, this term takes the classical form $\Psi(z, t) = \zeta \exp[-z^2/(4D_e t)]/\sqrt{\pi D_e t}$, where z is the perpendicular distance (in the gold) from the excited interface (see Fig. 1)²². For the cases of a single film or two contacting films, a solution can be obtained by considering successive reflections of the diffusion wave front at the film interfaces, where the non-equilibrium electron flux vanishes and its effective reflection coefficient is -1 . Electron reflection at the gold/gold interface depends on the contact, so we define an effective reflection coefficient r_f that lies between 0 (perfect transmission) and -1 (perfect reflection). The appropriate solution for $\Psi(z, t)$ at the surface ($z = 0$) for the non-contacting case of a film of thickness d is in the same form as that of the analogous thermal diffusion problem³¹:

$$\begin{aligned} \Psi(0, t) &= \frac{\zeta}{\sqrt{\pi D_e t}} \sum_{m=0}^{\infty} \exp\left(-\frac{(2dm)^2}{4D_e t}\right) \\ &= \frac{\zeta}{\sqrt{\pi D_e t}} \sum_{m=0}^{\infty} \beta^{m^2} = \frac{\zeta}{2\sqrt{\pi D_e t}} [1 + \mathcal{I}_3(0, \beta(d, t))], \end{aligned} \quad (2)$$

where $\mathcal{I}_3(0, \beta)$ is a Jacobi theta function and $\beta(d, t) = \exp[-(2d)^2/(4D_e t)]$. The corresponding equation for the case of two films of thickness d in imperfect contact is

$$\Psi_{r_f}(0, t) = \frac{\zeta}{2\sqrt{\pi D_e t}} \sum_{m=0}^{\infty} \{1 + [-(1 + 2r_f)]^m\} \beta^{m^2}. \quad (3)$$

This reduces to Eq. (2) when $r_f = -1$. The predicted ratio $\Psi_{r_f}(0, \tau_R)/\Psi(0, \tau_R)$, shown in Fig. 3(a) vs r_f , varies from the expected value of 1.0 when $r_f = -1$ to 0.575 when $r_f = 0$. For the simple case of perfect contact one can use Eqs. (2) and (3) to estimate the corresponding normalized spike height at $z = 0$ for two films of thickness $d = 37$ nm at $t = \tau_R = 0.9$ ps: $\Psi_{r_f=0}(0, \tau_R)/\Psi(0, \tau_R) \approx 0.58$, in good agreement with experiment in Fig. 3(c) for $p \geq 0.5$ GPa.

Discussion

In order to derive the real contact area S_r at any pressure p , one requires a model that relates S_r to r_f and to p . Assuming plastic flow of non-interacting microscopic gold asperities^{32,33}, the ratio between the real (S_r) and nominal (S_0) contact areas can be expressed as a function of p by the following empirical equation: $S_r/S_0 = p/(p + H)$ for loads up to and greater than H , where H is the Vickers hardness, as shown in Fig. 3(b). (This is an approximation for more complicated theories^{34,35}.) In addition, we expect r_f to be determined by the

ratio between the real and nominal contact areas through $S_r/S_0 = 1 - |r_f| = 1 + r_f$ assuming that the interstitial air gaps prevent electron transport and that asperity-to-asperity contact is perfect. The former assumption is reasonable considering the ~ 2 nm surface roughness of our gold films (i.e. \gg sub-nm tunneling distances); likewise for the latter assumption, considering that gold does not form an oxide layer. By least-squares fitting of $\Psi_{r_f=-H/(p+H)}(0, \tau_R)/\Psi(0, \tau_R)$ for all data sets using H as a fitting parameter, the best fit is obtained with $H = 0.24 \pm 0.10$ GPa, as shown by the solid curves in Fig. 3(c). The weighted average of the data in Fig. 3(c) is shown by the dotted curve in Fig. 3(d), giving excellent agreement with the theory (solid curve), including the reproduction of the downward slope. (The weighting was done in inverse proportion to the standard deviations. The variations in the thermal diffusivity of electrons in gold with pressure are estimated not to significantly contribute to the observed changes in spike height. See Ref. 36.) This value of H is consistent with that, $0.15 < H \leq 2$ GPa, reported for gold^{37,38}. Our results thus provide strong evidence that ultrafast electron diffusion can indeed directly map the real (asperity) contact area S_r , in the range from $S_r/S_0 = 0$ to the maximum probed value ~ 0.85 .

In conclusion, we have mapped nanoscale-roughness mechanical contacts from transient optical reflectivity changes on femtosecond time scales. By modelling the dynamics of electrons diffusing between contacting metal asperities and using an empirical relation between the real contact area, the hardness and the contact pressure, we demonstrate how the real contact area of a nanoscale contact can be probed *in situ* during loading and unloading. Accessing the real contact area is possible thanks to the insulating spaces between the contacting surfaces, forcing the diffusing electrons to pass only through the meshed nano-asperities. Compared to optical methods for probing the real contact area the present method allows samples with much smaller roughness, down to angstrom-order, to be accessed. At present we are limited to a lateral spatial resolution of ~ 1 μm , but this could be improved by the use of shorter optical wavelengths or near-field optical methods. In future it would be interesting to probe interfaces between different transparent substrates and metal films; films with greater hardness than gold would, in particular, allow better access to the poor-electrical-contact (low $|r_f|$) region. The method can also be extended to Vickers indenters or other types of indenter or to planar contacts. By such direct, local measurements of transient optical reflectivity changes at contacts, this study not only opens the way to the physics of ultrafast electron diffusion across contacting surfaces and inside asperities, with applications in microelectronic devices, but also to the mapping of the real contact area of nanoscale mechanical contacts, invaluable for accessing the underlying mechanisms for adhesion, friction and wear.

Methods

The frequency-doubled probe beam passes through a delay line, and is focused together with the infrared pump beam from below onto the interface between the sapphire plate and the gold film with a $\times 50$ objective lens (numerical aperture 0.35, working distance 18 mm). Pump and probe spot diameters are 1.0 and 1.1 μm (intensity at e^{-2} , respectively, with corresponding fluences 11 and 3 J/m² (resulting in steady state temperature rises in and out of contact ~ 8 and 16 K, respectively).

The optical reflectivity changes of the probe beam are monitored as a function of the time delay t between the pump and probe pulses. The pump beam is chopped at a frequency of 1 MHz for synchronous lock-in detection. The probe reflectivity change, coupled to the non-equilibrium electron distribution, varies linearly with the pump fluence up to the value used. Image data is obtained from the difference in the transient reflectivity change at delay times $t = -1$ ps and $\tau_R = 0.9$ ps (the spike height). This image data is obtained by scanning the objective lens laterally in two dimensions over the contact area.

The gold films, of thickness 37 nm, are chosen to be reasonably thick compared to the ~ 10 nm optical absorption depth of the ultrashort light pulses while at the same time being smaller than the ~ 100 nm electron diffusion depth¹⁴.

1. Johnson, K. L. *Contact mechanics* (Cambridge University Press, Cambridge, UK, 1985).



2. Swain, M. V. Mechanical property characterisation of small volumes of brittle materials with spherical tipped indenters. *Mat. Sci. Eng.* **A253**, 160–166 (1998).
3. Bobji, M. S., Pethica, J. B. & Inkson, B. J. Indentation mechanics of cu-be quantified by an in situ transmission electron microscopy mechanical probe. *J. Mater. Res.* **20**, 2726 (2005).
4. Kendall, K. & Tabor, D. An ultrasonic study of the area of contact between stationary and sliding surfaces. *Proc. R. Soc. Lond. A* **323**, 321–340 (1971).
5. Drinkwater, B. W., Dwyer-Joyce, R. S. & Cawley, P. A study of the interaction between ultrasound and a partially contacting solid-solid interface. *Proc. R. Soc. Lond. A* **452**, 2613–2628 (1996).
6. Dehoux, T., Wright, O. B., Voti, R. L. & Gusev, V. E. Nanoscale mechanical contacts probed with ultrashort acoustic and thermal waves. *Phys. Rev. B* **80**, 235409 (2009).
7. Dehoux, T., Wright, O. B. & Voti, R. L. Picosecond time scale imaging of mechanical contacts. *Ultrasonics* **50**, 197 (2010).
8. Ovcharenko, A., Halperin, G., Verberne, G. & Etsion, I. In situ investigation of the contact area in elastic-plastic spherical contact during loading-unloading. *Tribol. Lett.* **25**, 153 (2007).
9. Rubinstein, S., Cohen, G. & Fineberg, J. Dynamics of precursors to frictional sliding. *Phys. Rev. Lett.* **98**, 226103 (2007).
10. Ben-David, O., Rubinstein, S. M. & Fineberg, J. Slip-stick and the evolution of frictional strength. *Nature* **463**, 76–79 (2010).
11. Brorson, S., Fujimoto, J. & Ippen, E. Femtosecond electronic heat-transport dynamics in thin gold films. *Phys. Rev. Lett.* **59**, 1962–1965 (1987).
12. Elsayed-Ali, H., Juhasz, T., Smith, G. & Bron, W. Femtosecond thermoreflectivity and thermotransmissivity of polycrystalline and single-crystalline gold films. *Phys. Rev. B* **43**, 4488 (1991).
13. Sun, C.-K., Vallée, F., Acioli, L. H., Ippen, E. P. & Fujimoto, J. G. Femtosecond-tunable measurement of electron thermalization in gold. *Phys. Rev. B* **50**, 15337–15348 (1994).
14. Wright, O. B. Ultrafast nonequilibrium stress generation in gold and silver. *Phys. Rev. B* **49**, 9985–9988 (1994).
15. Qui, T., Juhasz, T., Suarez, C., Bron, W. E. & Tien, C. Femtosecond laser heating of multi-layer metals ii. experiments. *Int. J. Heat Mass Transfer* **37**, 2799–2808 (1994).
16. Del Fatti, N. *et al.* Nonequilibrium electron dynamics in noble metals. *Phys. Rev. B* **61**, 16956 (2000).
17. Hostetler, J., Smith, A., Czajkowsky, D. & Norris, P. Measurement of the electron-phonon coupling factor dependence on film thickness and grain size in au, cr, and al. *Appl. Opt.* **38**, 3614–3620 (1999).
18. Hohlfeld, J. *et al.* Electron and lattice dynamics following optical excitation of metals. *Chem. Phys.* **251**, 237–258 (2000).
19. Guo, C., Rodriguez, G. & Taylor, A. Ultrafast dynamics of electron thermalization in gold. *Phys. Rev. Lett.* **86**, 1638–1641 (2001).
20. Kruglyak, V., Hicken, R., Matousek, P. & Towrie, M. Spectroscopic study of optically induced ultrafast electron dynamics in gold. *Phys. Rev. B* **75**, 035410 (2007).
21. Tas, G. & Maris, H. J. Electron diffusion in metals studied by picosecond ultrasonics. *Phys. Rev. B* **49**, 15046 (1994).
22. Gusev, V. & Wright, O. B. Ultrafast nonequilibrium dynamics of electrons in metals. *Phys. Rev. B* **57**, 2878 (1998).
23. Bron, W., Guerra III, A. & Suárez, C. Imaging through quasi-particle transport. *Opt. Lett.* **21**, 997–999 (1996).
24. Palik, D. & Ghosh, G. *Electronic Handbook of Optical Constants of Solids* (Academic, San Diego, 1999).
25. Lin, Z., Zhigilei, L. V. & Celli, V. Electron-phonon coupling and electron heat capacity of metals under conditions of strong electron-phonon nonequilibrium. *Phys. Rev. B* **77**, 075133 (2008).
26. Oliver, W. C. & Pharr, G. M. An improved technique for determining hardness and elastic modulus using load and displacement sensing indentation experiments. *J. Mater. Res.* **7**, 1564–1583 (1992).
27. Anderson, O. L. Determination and some uses of isotropic elastic constants of polycrystalline aggregates using single-crystal data. In Mason, W. P. (ed.) *Physical Acoustics*, vol. 3B (Academic Press, New York, 1965).
28. Jaffar, M. J. A general solution to the axisymmetric frictional contact problem of a thin bonded elastic layer. *Proc. Inst. Mech. Eng.* **211**, 549–57 (1997).
29. Yu, H. Y., Sanday, S. C. & Rath, B. B. The effect of substrate on the elastic properties of films determined by the indentation test. Axisymmetric Boussinesq problem. *J. Mech. Phys. Solids* **38**, 745–764 (1990).
30. Matsuda, O. & Wright, O. B. Reflection and transmission of light in multilayers perturbed by picosecond strain pulse propagation. *J. Opt. Soc. Am. B* **19** (2002).
31. Carslaw, H. & Jaeger, J. *Conduction of Heat in Solids* (Oxford University Press, 1959).
32. Madhusudana, C. V. *Thermal contact conductance* (Springer, New York, 1996).
33. Mikić, B. Thermal contact conductance; theoretical considerations. *Int. J. Heat Mass Transfer* **17**, 205–214 (1974).
34. Luan, B. & Robbins, M. O. The breakdown of continuum models for mechanical contacts. *Nature* **435**, 929–932 (2005).
35. Persson, B. N. J. Contact mechanics for randomly rough surfaces. *Surf. Sci. Rep.* **61**, 201–227 (2006).
36. Sundqvist, B. & Bäckström, G. Thermal conductivity of gold and silver at high pressures. *J. Phys. Chem. Solids* **39**, 1133–1137 (1978).
37. Persch, G., Born, C. & Utesch, B. Nano-hardness investigations of thin films by an atomic force microscope. *Microelectron. Eng.* **24**, 113–121 (1994).
38. Lucas, M., Gall, K. & Riedo, E. Tip size effects on atomic force microscopy nanoindentation of a gold single crystal. *J. Appl. Phys.* **104**, 113515–113515 (2008).

Acknowledgments

We thank Roberto Li Voti for stimulating discussions.

Author contributions

M.T. and O.B.W. wrote the main manuscript text. Y.I., T.D., and M.T. contributed to the measurements. M.T. and Y.I. prepared the samples. V.E.G., M.T., O.M. and O.B.W. contributed to the theory. All authors reviewed the manuscript.

Additional information

Supplementary information accompanies this paper at <http://www.nature.com/scientificreports>

Competing financial interests: The authors declare no competing financial interests.

How to cite this article: Tomoda, M. *et al.* Nanoscale mechanical contacts mapped by ultrashort time-scale electron transport. *Sci. Rep.* **4**, 4790; DOI:10.1038/srep04790 (2014).



This work is licensed under a Creative Commons Attribution-NonCommercial-NoDerivs 3.0 Unported License. The images in this article are included in the article's Creative Commons license, unless indicated otherwise in the image credit; if the image is not included under the Creative Commons license, users will need to obtain permission from the license holder in order to reproduce the image. To view a copy of this license, visit <http://creativecommons.org/licenses/by-nc-nd/3.0/>